46th AIAA Plasmadynamics and Lasers Conference AIAA-2015-3246
22–26 June 2015, Dallas, TX

Aero-Optical Measurements of High-Mach Supersonic Boundary Layers

Stanislav Gordeyev[1], R. Mark Rennie[2],
Department of Aerospace and Mechanical Engineering,
University of Notre Dame, Notre Dame, Indiana, 46545

Alan B. Cain[3]
Innovative Technology Applications Co., (ITAC), LLC
Chesterfield, MO, 63006

and

Timothy E. Hayden[4]
Department of Aeronautics,
U.S. Air Force Academy, Colorado Springs, Colorado 80840

Aero-optical measurements of a boundary layer at high supersonic speeds of M = 3.0 and 4.3 were performed in the Trisonic Wind Tunnel at the US Air Force Academy. Overall levels of aero-optical distortions, convective speeds and the aperture functions were calculated from the data. It was found that the statistics of the aero-optical distortions were similar to subsonic boundary layers. Several modified models were shown to properly predict aero-optical levels of boundary layers up to M = 5. As a separate experiment, a wedge model was placed inside the tunnel to study the aero-optical effects of the attached oblique shock. Aero-optical structures with an abnormally-low convective speed were observed in the laser beam traversing the oblique shock around the wedge. These structures were speculated to be related to convecting unsteady distortions imposed on the oblique shock by the naturally-vibrating wedge.

I. Introduction

AERO-OPTICAL effects are the result of the dependence of the index-of-refraction, n, on the density in air, ρ, via the Gladstone-Dale constant, K_{GD} (which is approximately 2.27×10^{-4} m^3/kg in air for visible wavelengths of light), $n(\vec{x},t)-1=K_{GD}\rho(\vec{x},t)$. Light passing through regions of unsteady turbulent flow is distorted by the spatially- and temporally-fluctuating density fields present along the optical path length. For transonic, supersonic and hypersonic flows, this effect poses a significant problem for the performance of airborne optical systems, whether they are directed energy, imaging, or free-space communications applications, as disturbances to optical wavefronts in the near-field will result in significant reductions in both time-averaged and instantaneous on-target intensities [1,2].

[1] Research Associate Professor, Department of Mechanical and Aerospace Engineering, Hessert Laboratory for Aerospace Research, Notre Dame, IN 46556, AIAA Associate Fellow.
[2] Research Associate Professor, Department of Mechanical and Aerospace Engineering, Hessert Laboratory for Aerospace Research, Notre Dame, IN 46556, Senior Member AIAA.
[3] President, Innovative Technology Applications Company, Chesterfield, MO 63006, Associate Fellow AIAA.
[4] Aerospace Engineer, Department of Aeronautics, Senior Member AIAA.

The effect of turbulent density fluctuations on the propagation of light can be quantified by defining the Optical Path Difference (OPD) as the average-removed integral of the index-of-refraction of a medium along the physical length traversed by a ray of light,

$$OPD(x,y,t) = \int n'(x,y,z,t)dz = K_{GD} \int \rho'(x,y,z,t)dz$$

where primes denote mean-removed fluctuations and z is the direction of beam propagation.

One of the important fundamental flows responsible for aero-optical aberrations is the turbulent boundary layer (BL) [2]. While the turbulence levels inside turbulent boundary layers are smaller than the turbulence intensity downstream of turrets, boundary layers, especially at transonic and supersonic speeds, cause significant aero-optical distortions causing an efficiency degradation in directed energy systems [2,3,4] or disrupting free-space high-bandwidth airborne communication systems [5]. In addition, studying time-resolved aero-optical distortions provides valuable information into the dynamics of large-scale structures of the turbulent boundary layer [3].

While the aero-optics of subsonic boundary layers has been extensively studied in recent years [2,3 and references therein], experimental measurements [4,6,7] and numerical simulations [8,9,10] of aero-optical effects in supersonic boundary layers are very limited and many important questions about the details of the underlying aero-optical structure and its dynamics still remain unanswered. Several theoretical models were proposed [4,6] to predict levels of aero-optical distortions caused by supersonic boundary layers at different Mach and Reynolds numbers, but additional experimental data are needed to fully verify them at high supersonic speeds.

II. Experimental Set-Up

All aero-optical measurements were performed in the Trisonic Wind Tunnel, US Air Force Academy, Colorado Springs. The tunnel is an open circuit, blowdown-type facility, with a range of Mach numbers between 0.24 - 4.5. The supply air is dried using desiccant drying towers and is compressed by two rotary screw compressors of 350 hp each. The tunnel has a 1 ft x 1 ft cross-section test section with two 12” round optical windows on both sides of the test section.

The aero-optical distortions caused by turbulent boundary layers were measured using two nozzle inserts at test section Mach numbers of 4.3 and 3.0; to change the test section freestream density the plenum pressure was varied between 75 and 220 psi. To monitor the flow condition, the plenum is instrumented with total pressure and total temperature sensors, as well as with a static pressure sensor, installed upstream of the test section window. The freestream density was calculated using the total temperature and pressure measurements and the isentropic relation. A summary of test conditions for all runs is given in Table 1.

All measurements were performed using a high-speed Shack-Hartmann WaveFront Sensor, WFS; a photograph and schematic of the experimental set-up are shown in Figure 1. The laser beam, after passing through a 1-inch beam expander and, in some cases through an expanding telescope to expand the beam to 2-inch, was forwarded into the test section normal to the optical window. The return mirror on the other side of the test section reflected the beam back to the optical table exactly the same way as it was projected into the test section. The incoming beam, after passing through the expanding telescope was split off using a cube beam splitter and, after passing through two focusing lens, was sent to a high-speed digital camera, Phantom v1610. The camera had a 38 mm focal length, 70 x 60 lenslet array attached, and aero-optical distortions were collected at different sampling speeds and spatial resolutions, see Table 1.

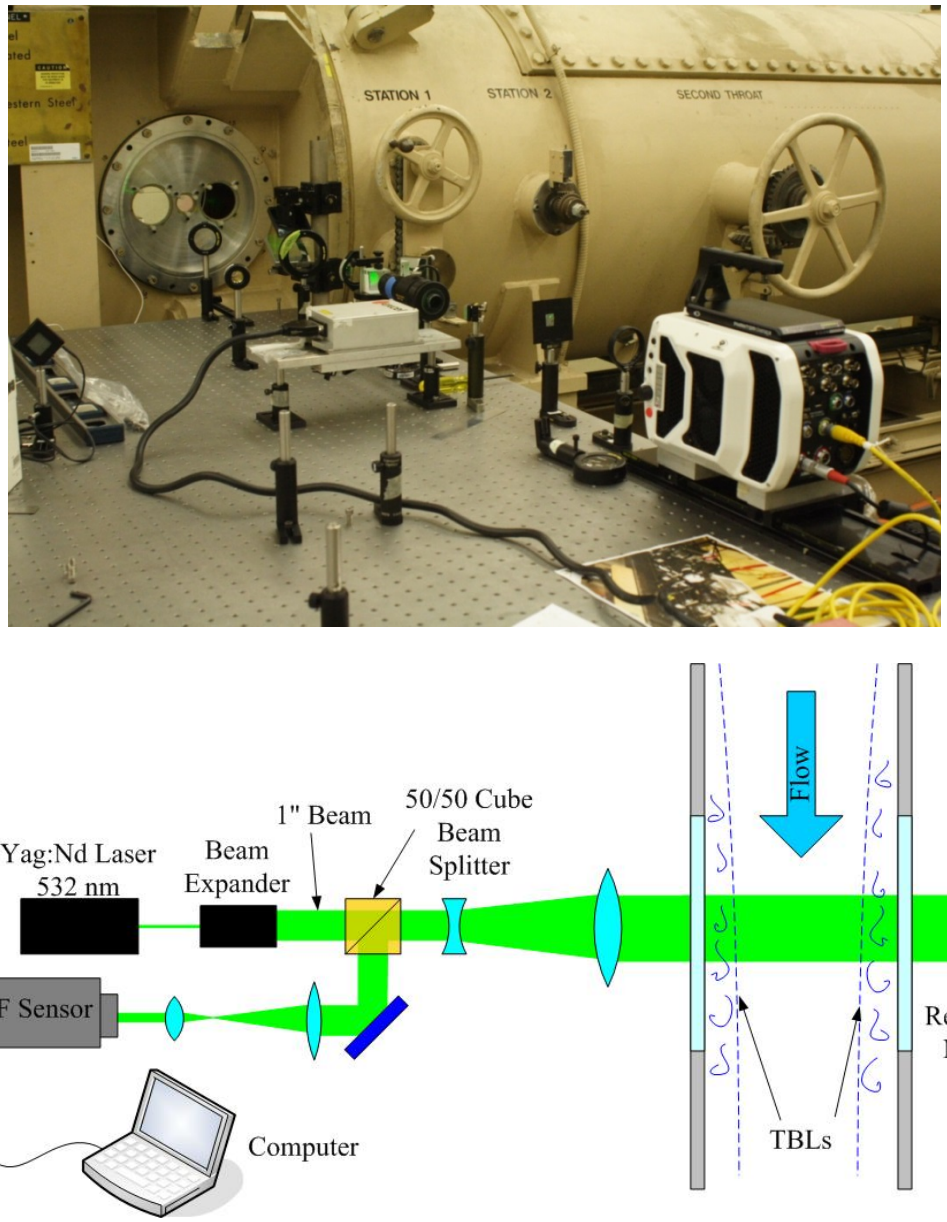

Figure 1. Photograph (top) and schematic (bottom) of BL experimental set-up using WFS.

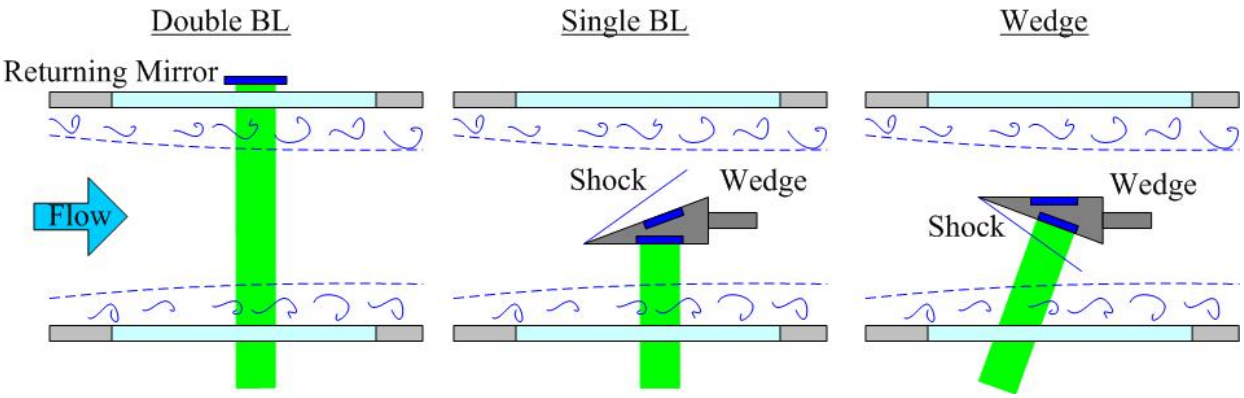

Figure 2. Schematics of different BL laser beam arrangements.

Table 1. Flow parameters and measurement information for all cases.

Case	M_∞	P_0, MPa (psi)	T_0, K	ρ_∞, kg/m^3	Ap, mm	WF size	fs_{amp} , Hz
DBLM4-1	4.3	1.489 (216)	305	0.366	50	41 x 41	49,008
DBLM4-M1	4.3	1.517 (215)	304	0.373	50	11 x 1	646,153
DBLM3-1	3.0	1.317 (191)	304	1.15	50	41 x41	49,008
DBLM3-M1	3.0	0.676 (98)	304	0.591	50	11 x 1	646,153
DBLM3-M2	3.0	1.020 (148)	302	0.897	50	11 x 1	646,153
DBLM3-4	3.0	1.000 (145)	307	0.865	50	41 x 41	49,008
WM3-1	3.0	0.524 (76)	301	0.462	50	41 x 41	49,008
WM3-M1	3.0	0.531 (77)	302	0.467	50	11 x 1	646,153
WM3-2	3.0	0.703 (102)	303	0.614	50	41 x 41	49,008
WM3-M2	3.0	0.827 (120)	303	0.725	50	11 x 1	646,153
SBLM3-1	3.0	0.703 (102)	301	0.620	50	70 x 53	33,018
SBLM3-M1	3.0	0.827 (120)	302	0.727	50	11 x 1	646,153

For both Mach numbers, the laser beam was passed into the empty test section normal to the test section window, so that it encountered two supersonic boundary layers on both sides of the test section. This test is later referred as the "double boundary-layer" test, see Figure 2, left. For the M = 3 case, two additional tests were performed with a 20-degree wedge model installed in the middle of the test section, with one side of the wedge parallel to the incoming flow. Both sides of the wedge had flush-mounted 2-inch round mirrors. The locations of both mirrors are superimposed on a Schlieren image of the flow around the wedge at M = 4.3, see Figure 3.

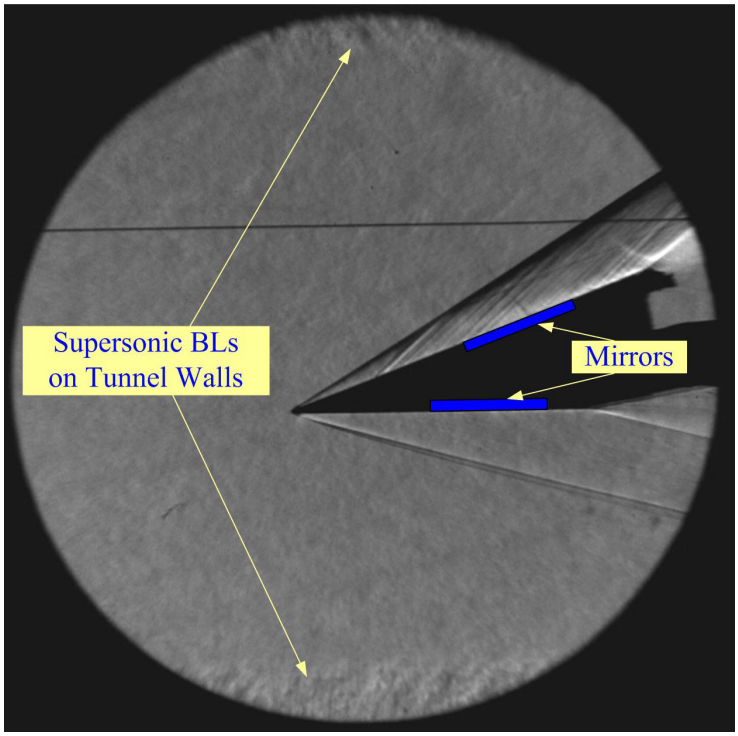

Figure 3. Schlieren picture of the flow around the wedge for M = 4.3. Actual positions of the mirrors are also shown.

In the first additional test, the wedge was positioned with the parallel-to-flow side vertical and facing the incoming beam. The laser beam was reflected from the mirror back to the optical table exactly along the same way it came into the test section. In this test the beam traversed normally through only one boundary layer and this test will be later called the "single boundary-layer" test, as shown in Figure 2, middle.

During the second additional test, the wedge was positioned vertically with the 20-degree side facing the optical table and the laser beam was again reflected off the mounted mirror back to the optical table. To do this, the laser beam was tilted downstream 20 degrees off the normal direction, going at an oblique angle through the single boundary layer, see Figure 2, right. Also, the beam traversed through the shock formed by the presence of the wedge. This test will later be called the "Wedge" test.

III. Data Collection and Reduction

Wavefront data were measured in two different ways. Aberrations over the full beam were collected with different spatial resolutions, an example of a 41 x 41 dots image is shown in Figure 4, top. This set of measurements allows studying the detailed spatial variation of BL-related aberrations, but only for a fixed aperture size of 50 mm, see Table 1.

Two-dimensional wavefronts were reduced using in-house software to obtain temporal sequences of wavefronts as a function of location in the aperture and time, $W = W(x, y, t)$. Residual tip/tilt was removed from the wavefronts through least-squares plane fitting, and the steady lensing was removed by removing the spatial mean of the wavefront. The optical path difference (OPD) is the conjugate of the wavefront, $OPD(x, y, t) = -W(x, y, t)$. For each test condition, a time-averaged spatial variation of the OPD across the aperture was computed, $\overline{OPD_{RMS}(Ap) = \sqrt{\langle OPD(x, y, t)^2 \rangle_{(x,y)}}}$. Here angled brackets denote spatial averaging over the aperture and the overbar denotes time-averaging.

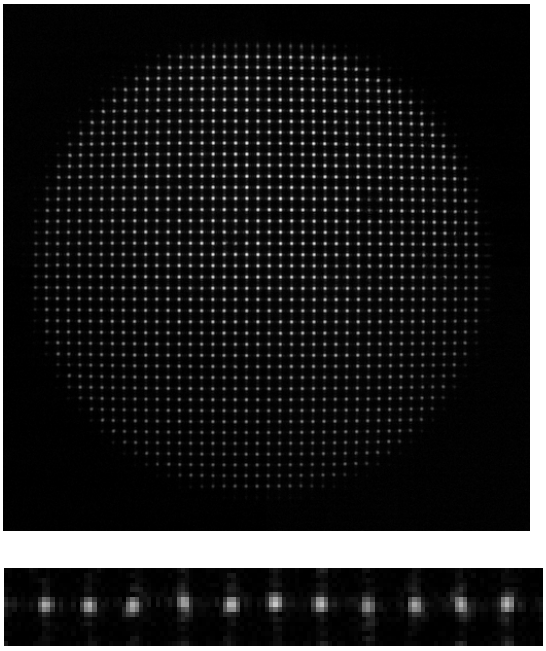

Figure 4. Top: Full 2-D wavefront image. Bottom: 11 x 1 wavefront image.

In addition to the full-aperture wavefronts described above, only a small portion of the dot pattern consisting of a streamwise line of 11 dots, see Figure 4, bottom, was sampled at a much higher sampling rate of 646,153 frames-per-second, see Table 1. These measurements are essentially equivalent to measurements using a multi-beam Malley probe [3]. Using a multi-point cross-correlation technique, outlined in [7], the convective speed of aero-optical structures and the corresponding traveling portion of the deflection angle spectrum, $\theta_T(f)$, can be found. Using the frozen field assumption, various important characteristics of the BL-related aero-optical distortions, such as an overall level of aero-optical distortions, OPD_{rms} and the aperture function, $G(Ap)$, can be calculated [3],

$$OPD_{rms}^2 = 2U_c \int_0^\infty \frac{\left|\hat{\theta}_T(f)\right|^2}{(2\pi f)^2} df \tag{1a}$$

$$G(Ap/\delta) \equiv OPD_{rms}(Ap)/OPD_{rms}, \quad \text{where}$$

$$OPD_{rms}^2(Ap) = 2U_c \int_0^\infty AF(Ap, f) \frac{\left|\hat{\theta}(f)\right|^2}{(2\pi f)^2} df \tag{1b}$$

The boundary layer thicknesses for both Mach numbers were estimated using the geometry of the nozzles and a semi-empirical method presented in [11]. Using the nozzle geometry, the streamwise Mach number distribution, $M(x)$, was calculated. Using the Mach number distribution, the method [11] calculates the streamwise growth of the boundary layer by estimating an equivalent flat plate length, $X(x)$,

$$X(x) = P(x)^{-1} \int_0^x P(x)dx, \quad \text{where}$$

$$P(x) = \left[M(x)/(1+0.2M(x)^2)\right]^4$$

$$R_X(x) = (a_0/\nu_0)X(x)M(x)(1+0.2M(x)^2)^{-(3-\omega)}$$

Here $R_X(x)$ is the equivalent Reynolds number, corresponding to X, a_0 and ν_0 are the stagnation speed of sound and the dynamic viscosity, respectively, and ω is the exponent in the viscosity-temperature relation, here $\omega = 0.75$ was used. Using $X(x)$, $R_X(x)$ and stagnation values from Table 1, the boundary layer thickness can be computed for freestream Reynold numbers of the order of 10^7,

$$\delta(x) = 0.23X(x)R_X(x)^{-1/6}.$$

Similarly, for large Reynolds numbers, the momentum and displacement thicknesses can be calculated from $X(x)$ and $R_X(x)$ as [11],

$$\theta(x) = 0.022(1+0.1M(x)^2)^{-0.7} X(x)R_X(x)^{-1/6}$$

$$\delta^*(x) = 0.028(1+0.8M(x)^2)^{0.44} X(x)R_X(x)^{-1/6}$$

The accuracy of the presented method was estimated to be within 10% at M = 3 [11].

For M = 3 the thickness of the BL at the measurement location was estimated to be 16 ± 1.5 mm for all stagnation conditions and for M = 4.3 the thickness was found to be 26 ± 2.5 mm. For M = 3, Re_θ was between 50,000 (P_0 = 98 psi) and 110,000 (P_0 = 191 psi) and for M=4.3, Re_θ = 43,000.

The same boundary layer analysis was performed for M = 2 supersonic boundary layer experiments, reported in [4] and it was found that the boundary layer thickness was 10 mm, and not 12 mm, as it was reported in [4]. In [4] Schlieren images were also used to estimate the boundary layer thickness; however, it is difficult to estimate errors from the Schlieren images. As such, an updated BL thickness of 10 mm will be used later in this paper when comparing the results from [4] with the present results.

The local skin friction at the measurement location, C_f, was estimated by calculating the incompressible skin friction, $C_{f,i}$, using several empirical expressions from [12], namely the Cole-Fernholz Methods 1, 2 and the White method, (note that all methods produced results within 5%) and correcting for compressibility effects [11], $C_f = C_{f,i} \cdot (1+0.1M^2)^{-0.7}$.

IV. Results

BL experiments

Two deflection angle amplitude spectra for different freestream densities for M = 3 and one deflection angle spectrum for M = 4.3, normalized by $\rho_\infty \delta M_\infty^2 F(M_\infty)$ (the empirical function $F(M_\infty)$ is presented in Figure 8), are shown in Figure 5. The subsonic deflection angle spectrum from [3] is also shown for comparison. The spectra for M = 3 collapse well onto each other, confirming that the aero-optical distortions, for a fixed Mach number, are proportional to $\rho_\infty \delta$. All spectra have a peak at approximately $St_\delta = 0.9$. This is a very useful result, as it provides a non-intrusive means to measure the boundary layer thickness over a wide range of Mach numbers by sending a small-aperture laser beam normal to the boundary layer and finding the location of the peak in the deflection angle spectrum.

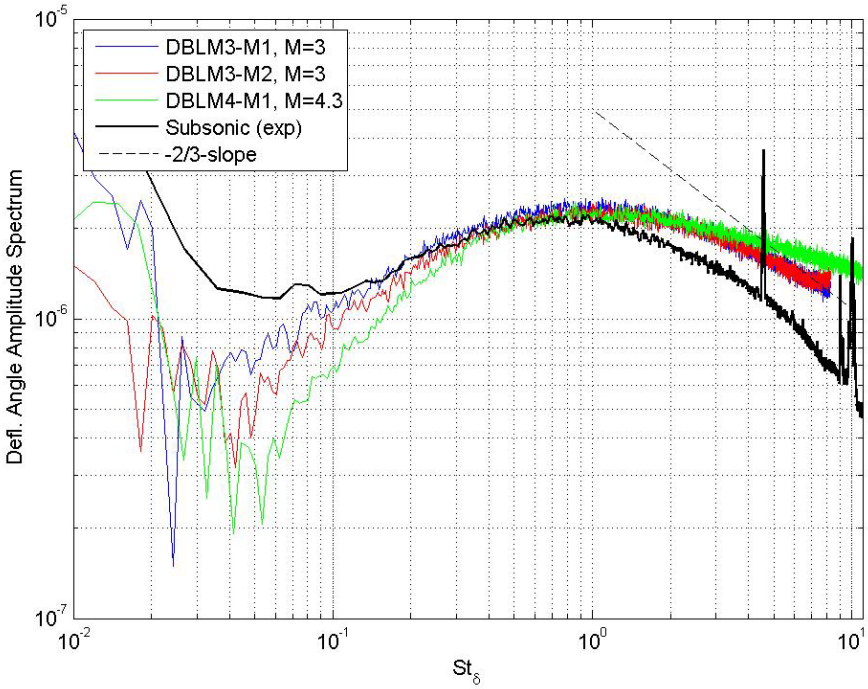

Figure 5. Normalized deflection angle spectra for M = 3 and M = 4.3. A subsonic spectrum from [3] is also shown for comparison.

At the low end of the spectrum, $0.05 < St_\delta < 1$, which corresponds to large-scale structures, the deflection-angle amplitude decreases as the Mach number increases. At the high-end of the spectra, $St_\delta > 1$, the trend is the opposite: energy in the small-scale structures increases with increasing Mach number. At this point, it is not clear why this is the case, as numerical simulations of boundary layers in a wide range of Mach numbers between 2.5 and 20 [16] did not show any significant changes in the streamwise velocity correlations.

At high frequencies, both the subsonic and M = 3 spectra approach the slope of $f^{2/3}$, which was shown to correspond to small-scale structures in the energy-cascade region [3]. The spectrum for M = 4.3, at least in the measured frequency range, does not approach this slope, which can be contributed to spectral blockage effects.

Using the deflection angle spectra, aperture functions were calculated, using Eq. 1(b), and are shown in Figure 6. While there are some differences, Figure 6 shows that the aperture functions for boundary layers are quite similar over a wide range of Mach numbers.

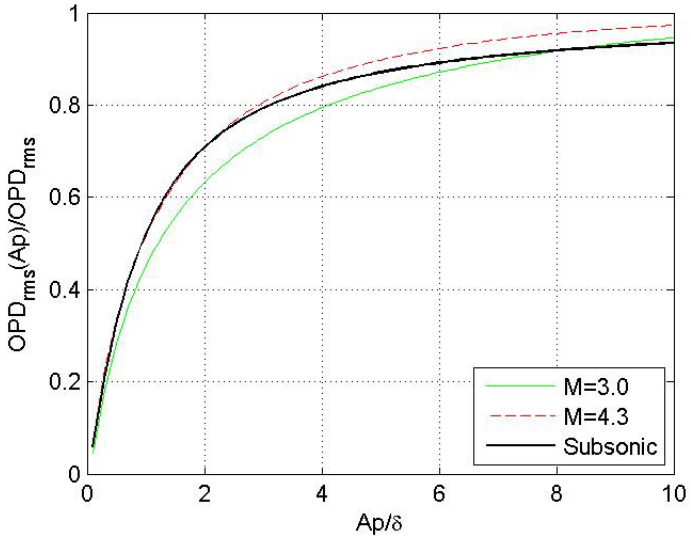

Figure 6. Aperture functions, $G(Ap/\delta)$, for tested supersonic Mach numbers, compared with the subsonic aperture function [3].

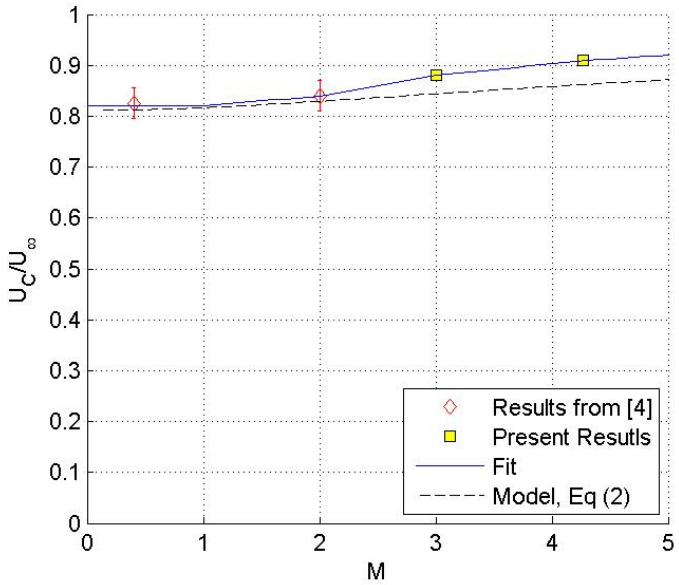

Figure 7. Experimentally-measured normalized convective speeds of aero-optical structures.

By cross-correlating deflection angles in the spectral domain, the convective speeds of aero-optical distortions were extracted and the results are presented in Figure 7, along with experimental results from [4]. Convective speeds are observed to monotonically increase with the Mach number, from $0.82U_\infty$ at subsonic speeds to $0.9U_\infty$ at M = 4.3. This effect was also observed in [4]. In [4,13] a model for boundary-layer aero-optical distortions was developed. Using the model, a simple model n for the convective speed was proposed,

$$\frac{U_C}{U_\infty} = \frac{\int \rho_{rms}(y)\left(\overline{U}(y)/U_\infty\right)dy}{\int \rho_{rms}(y)dy} \tag{2}$$

The convective velocity predicted by Eq (2) is also plotted in Figure 7 and shows good qualitative agreement with the experiments. The model presented in Refs. [4,13] showed that density fluctuations for supersonic speeds were suppressed near the wall due to higher flow temperatures near the wall and, therefore, aero-optical structures near the wall were less "optically" visible. Thus, aero-optical structures away from the wall were relatively stronger, resulting in higher observed aero-optical convective speeds at supersonic speeds. In [14] numerical simulations of aero-optical distortions for Mach numbers of 0.9 and 2.3 were performed and it was also observed that, while for the M = 0.9 case density fluctuations were approximately constant throughout the boundary layer, for the M = 2.3 case, density fluctuations in the outer part of the boundary layers were stronger than the ones near the wall. Similar trends of the wall-normal distribution of the density fluctuations were observed in [15], where supersonic boundary layers at M = 3, 4.5 and 6 were numerically simulated.

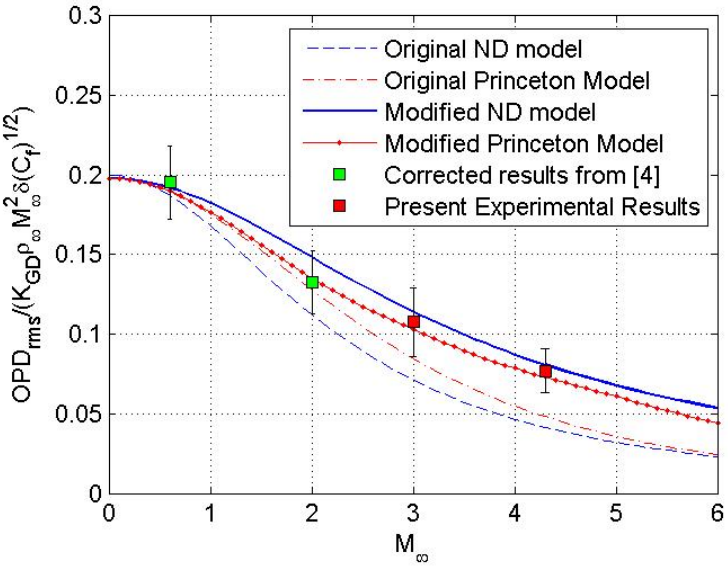

Figure 8. Normalized levels of OPDrms and predictions from different models.

Knowing the convective speeds and the deflection-angle spectra, OPD_{rms} can be calculated from 1-D wavefronts using Eq. (1a). Using the aperture functions in Figure 6, OPD_{rms} were also calculated from experimental 2-D wavefronts as $OPD_{rms} = OPD_{rms}(Ap)/G(Ap/\delta)$. For each Mach number, all OPD_{rms} values were averaged and the results, normalized by $K_{GD}\rho_\infty M_\infty^2 \delta\sqrt{C_f}$, are plotted in Figure 8, along with the experimental results from [4] using the updated value of the boundary layer thickness of 10 mm, as described before.

In [3,4] the following model for boundary-layer aero-optical distortions was derived,

$$OPD_{rms} = 0.2K_{GD}\rho_\infty M_\infty^2 \delta\sqrt{C_f}F(M_\infty), \tag{3}$$

where C_f is the compressible skin friction and $F(M_\infty)$ was numerically estimated from velocity measurements. This model with the F-function from [3,4] will be later called the "Original ND Model". A similar model was proposed in [6], which has the same functional form as Eq. (3), but with a different $F(M_\infty)$,

$$F(M_\infty) = \left(1 + 0.2M_\infty^2\left[1 - r(U_C / U_\infty)\right]\right)^{-3/2},$$

where $r = 0.89$ is the recovery coefficient and $U_C = 0.8U_\infty$ is the convective speed of aero-optical structures; this model will be called the "Original Princeton Model."

Predictions from both the Original ND and Original Princeton Models are plotted in Figure 8. Neither model properly predicts the present experimental data at higher Mach numbers. After revisiting both models it was concluded that the Original ND model incorrectly defined the relation between the compressible skin friction coefficient and the skin friction velocity and assumed that the wall temperature was equal to the total temperature, and not the recovery temperature. The Original Princeton model assumed that the convective speed of aero-optical distortions is constant, while both present and previous experimental results, summarized in Figure 6, indicate that it is a function of the freestream Mach number; this function was approximated by an empirical fit in Figure 7.

Both models were properly updated and the modified predictions are plotted in Figure 8. The two modified models now correctly predict the experimentally-observed OPDrms, and both of them can be used to predict the aero-optical effect of an adiabatic boundary layer over a wide range of Mach numbers between 0 and 5. Additional experimental data are needed to see whether the models correctly predict aero-optical distortions at even higher Mach numbers. An extension of ND model to non-adiabatic walls is presented in [13].

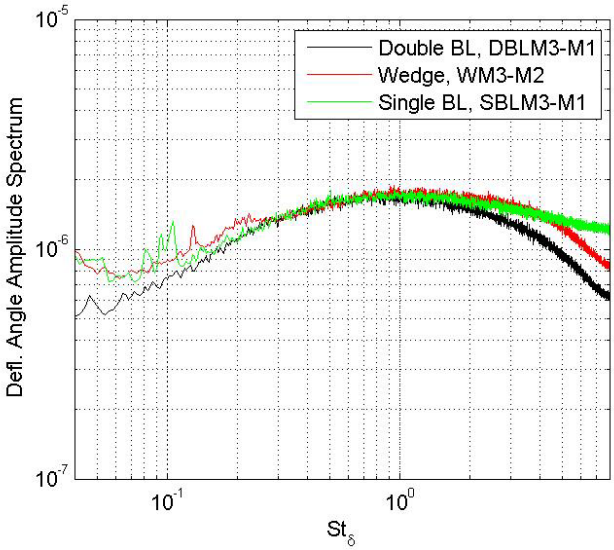

Figure 9. Properly normalized deflection angle spectra for different laser beam arrangements, as defined in Figure 2 and Table 1, for M = 3.

Wedge Experiments

Figure 9 presents deflection-angle spectra for the double-BL experiment, the single BL experiment and the wedge experiment. The double-BL spectrum was divided by $\sqrt{2}$ to factor out the effect of the beam passing through two BL's (assuming that the effects of the BL's on the two test-section walls are statistically independent). Both single BL and Wedge spectra have more energy at higher frequencies $St_\delta > 1$, most probably due to lower signal-to-noise and related spectral aliasing. Below $St_\delta = 1$, the spectra collapse fairly well, except around $St_\delta = 0.1$. Several sharp peaks in the single BL spectrum are due to mechanical vibrations of the wedge model. The

Wedge BL spectrum, in which the beam passed through the shock from the wedge, is consistently higher than the double BL and single BL spectra for St_δ between 0.1 and 0.3, or, in dimensional units, between 4 and 10 kHz. Analysis of the phase of the spectral cross-correlation, computed as discussed in [3] and shown in Figure 10, left plot, reveal that the aero-optical structures in this frequency range move at a much slower speed of approximately 230 m/s, compared to a higher speed of 562 m/s for the higher-frequency range. The higher speed was already associated with the aero-optical distortions inside the boundary layer on the tunnel wall, see a flow diagram in Figure 10, right. The low-frequency speed of 230 m/s, however, is too low to be explained by the presence of the boundary layers on the wedge or on the tunnel wall. Using the convective speed and the range of frequencies, the streamwise size of these slow-moving aero-optical structures are estimated to be on the order of 30 mm.

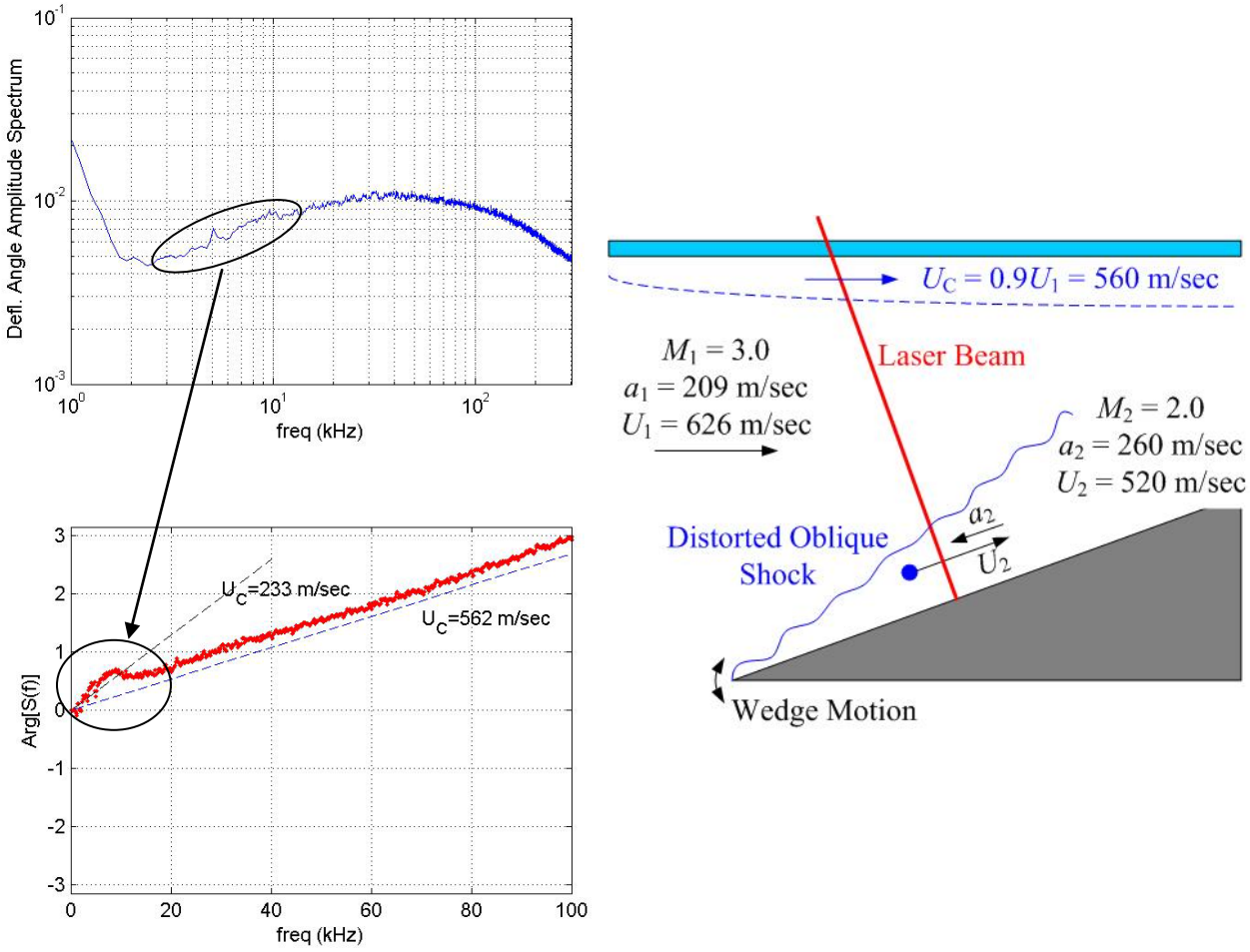

Figure 10. Left: Deflection angle spectrum (top plot) and a phase angle plot (bottom) for the wedge experiment WM3-M2. Convective speeds for different frequency ranges were calculated from the phase slope and given in the plot. Right: A diagram of the flow around the wedge for the incoming M = 3.0.

Note that the low-frequency range approximately corresponds to the range of mechanical vibrations of the wedge, observed in the single BL spectrum in Figure 9. As such, it is possible that the wedge motion generates spatial-temporal distortions of the oblique shock, as depicted in Figure 10, right. These spatial-temporal distortions would generate acoustical waves. The

"origin" of the waves would convect downstream with the freestream speed of U_2, while acoustical waves would propagate upstream with the local speed of sound, $-a_2$. The resulting speed of these distortions would be $U_2 - a_2$ = 520 m/sec – 260 m/sec = 260 m/sec, which is similar to the speed of 230 m/sec of the aero-optical structures observed in the low-frequency range, see Figure 10, left.

V. Conclusions

Experimental measurements of aero-optical distortions of the supersonic boundary layers were performed in the Trisonic Wind Tunnel at the US Air Force Academy for M = 3 and 4.3 and a variety of stagnation conditions. Wavefronts were measured using a high-speed wavefront sensor. Two types of measurements were performed, 2-D wavefronts with 49,000 fps rate and 1-D wavefronts with a higher sampling rate of 646,000 fps. Deflection angle spectra for both Mach numbers were shown to approximately collapse, with the peak location was found to be at St_δ = 0.9, independent of the incoming Mach number. Using the results of both measurements, the overall levels of aero-optical distortions were calculated for each experiment. Also, the aperture functions and convective speeds were extracted from the data. Convective speeds were observed to monotonically increase with Mach number. All experimental data were found to collapse on a single curve using the scaling proposed earlier, $OPD_{rms} = 0.2K_{GD}\rho_\infty M_\infty^2 \delta\sqrt{C_f}F(M_\infty)$. Discrepancies between the two existing models and experimental results at the measured Mach numbers were observed and modifications to both of the models were proposed; after these modifications, both models were able to correctly predict the overall levels of aero-optical distortions over a wide range of subsonic and supersonic boundary layers up to at least M = 5.

As a separate experiment, a wedge model with flush-mounted mirrors was installed in the test section in an attempt to quantify the aero-optical distortions caused by an attached oblique wave around the model. Weak slow-moving aero-optical structures were observed in the aero-optical data and a plausible mechanism explaining their low speed was provided.

Acknowledgments

This work has been supported by the United States Air Force Contract Number FA9550-13-C-0010. The U.S. Government is authorized to reproduce and distribute reprints for governmental purposes notwithstanding any copyright notation thereon. Any opinions, findings and conclusions or recommendations expressed in this material are those of the authors and do not necessarily reflect the views of the USAF.

References

[1] Jumper, E.J. and Fitzgerald, E.J., 2001, "Recent Advances in Aero-Optics," *Progress in Aerospace Sciences,* **37**, 299-339.

[2] Wang, M., Mani, A. and Gordeyev, S., "Physics and Computation of Aero-Optics", *Annual Review of Fluid Mechanics*, **44**, pp. 299-321, 2012.

[3] Gordeyev, S., Smith, A.E., Cress, J.A. and Jumper, E.J. "Experimental studies of aero-optical properties of subsonic turbulent boundary layers," *Journal of Fluid Mechanics*, **740**, pp. 214-253, 2014.

[4] Gordeyev, S., Jumper, E.J. and Hayden, T., "Aero-Optics of Supersonic Boundary Layers," *AIAA Journal*, **50**(*3*), 682-690, 2012.

[5] S. Gordeyev, J. Cress and E. Jumper, **"**Far-Field Laser Intensity Drop-Outs Caused by Turbulent Boundary Layers", *Journal of Directed Energy*, **5**(*1*), pp. 58-75, 2013.

[6] Wyckham, C. and Smits, A. "Aero-Optic Distortion in Transonic and Hypersonic Turbulent Boundary Layers,"*AIAA Journal*, **47**(*9*), pp. 2158-2168, 2009.
[7] A.E. Smith, S. Gordeyev, H. Ahmed, A. Ahmed, D.J. Wittich III and M. Paul, " Shack-Hartmann Wavefront Measurements of Supersonic Turbulent Boundary Layers in the TGF," AIAA Paper 2014-2493.
[8] E. Tromeur, E. Garnier and P. Sagaut, "Large-eddy simulation of aero-optical effects in a spatially developing turbulent boundary layer", *Journal of Turbulence*, **7**, 2006.
[9] E. Tromeur, P. Sagaut and E. Garnier, "Analysis of the Sutton Model for Aero-Optical Properties of Compressible Boundary Layers " *J. Fluids Eng.* **128**(*2*), 239-246, 2005.
[10] White, M. and Visbal, M., "Simulation of Aero-Optical Interactions in Transonic Boundary Layers," AIAA Paper 2011-3279, 2011.
[11] Stratford, B.S. and Beaver, G.S., *The Calculation of the Compressible Turbulent Boundary layer in an Arbitrary Pressure Gradient – A Correlation of Certain Previous Methods*, Reports and Memoranda No. 3207, Ministry of Aviation, Aeronautical Research Council, London, 1961.
[12] Nagib, H.M., Chauhan K.A. & Monkewitz P.A. "Approach to an asymptotic state for zero pressure gradient turbulent boundary layers," *Phil. Trans. R. Soc. A,* **365**, pp. 755-770, 2007.
[13] S. Gordeyev, J.A. Cress, A. Smith and E.J. Jumper, "Aero-Optical Measurements in a Subsonic, Turbulent Boundary Layer with Non-Adiabatic Walls", *Physics of Fluids*, **27**, 045110, 2015.
[14] E. Tromeur, E. Garnier, P. Sagaut and C. Basdevant, "Large eddy simulations of aero-optical effects in a turbulent boundary layer," *Journal of Turbulence*, **4**, 005, 2003.
[15] T. Maeder, N.A. Adams and L Kleiser, "Direct simulation of turbulent supersonic boundary layers by an extended temporal approach," *J. Fluid Mech*., **429**, pp. 187-216, 2001.
[16] M. Lagha, J. Kim, J. D. Eldredge, and X. Zhong, "A numerical study of compressible turbulent boundary layers," *Physics of Fluids*, **23**, 015106, 2011.